Icarus 421 (2024) 116219

Contents lists available at ScienceDirect

Icarus

journal homepage: www.elsevier.com/locate/icarus

Deep learning driven interpretation of Chang'E-4 Lunar Penetrating Radar

G. Roncoroni [a,*], E. Forte [a], I. Santin [a], A. Černok [a], A. Rajšić [b], A. Frigeri [c], W. Zhao [d], G. Fang [e,f,g], M. Pipan [a]

[a] Department of Mathematics, Informatics and Geosciences, University of Trieste, Italy
[b] Department of Earth, Atmospheric and Planetary Sciences, Purdue University, West Lafayette, IN, USA
[c] Istituto di Astrofisica e Planetologia Spaziali (IAPS), Istituto Nazionale di Astrofisica (INAF), Rome, Italy
[d] Key Laboratory of Geoscience Big Data and Deep Resource of Zhejiang Province, School of Earth Sciences, Zhejiang University, Hangzhou 310058, China
[e] Aerospace Information Research Institute, Chinese Academy of Sciences, Beijing 100190, China
[f] Key Laboratory of Electromagnetic Radiation and Sensing Technology, Chinese Academy of Sciences, Beijing 100190, China
[g] School of Electronic, Electrical and Communication Engineering, University of Chinese Academy of Sciences, Beijing 100049, China

ARTICLE INFO

Keywords:
Deep learning
LPR data
Interpretation
Attribute analysis
Data integration

ABSTRACT

We reprocessed Chang'E-4 Lunar Penetrating Radar data collected until 27th March 2023 with a total length of about 1440 m adding >400 m to the longest profile published so far. For data interpretation, we exploited a new Deep Learning-based algorithm to automatically extract reflectors from a processed radar dataset. The results are in terms of horizon probability and have been interpreted by integrating signal attribute analysis with orbital imagery. The approach provides more objective results by minimizing the subjectivity of data interpretation, allowing to link radar reflectors to their geological context and surface structures. For the first time, we imaged dipping layers and at least twenty shallow buried craterform structures within the regolith using Lunar Penetrating Radar data. We further recognized four deeper structures similar to craters, and identified a crater rim crossed by the rover path and visible in satellite imagery.

1. Introduction

One of the aims of the Chinese lunar landing mission Chang'E-4 (CE-4) is to identify mantle materials that could have been uplifted during the impact that created the South-Pole Aitken basin. As a part of this mission, the Yutu-2 rover landed on 3rd January 2019, on the lunar farside, in the pre-Nectarian Van Kármán crater (diameter D = 185 km; 177.5991°E, 45.4446°S), located within the South Pole-Aitken basin (SPA), the largest and likely the oldest impact structure on the Moon (Byrne, 2008) (Fig. Sup. S1, S2). Among all, two scientific targets of the Yutu-2 rover are: 1) to study the mineralogy of the SPA by collecting in situ reflectance spectra; and 2) image the subsurface shallow geology using a subsurface penetrating radar system. The Lunar Penetrating Radar (LPR) on Yutu-2 is the first radar moving directly on the surface of the Moon's farside (Dong et al., 2021). As in the Chang'E-3 (CE-3) mission, the fundamental goal of the LPR surveys in CE-4 was the exploration of the lunar subsurface structures along the rover's path, potentially down to several tens or even hundreds of meters (Fang et al., 2014; Jia et al., 2018; Wu et al., 2019). For these reasons, in addition to reflectance spectra and several other sensors, the Yutu-2 rover is equipped with a dual frequency Lunar Penetrating Radar (LPR) with dominant frequencies centered at 60 and 500 MHz (CH-1 and CH-2, respectively).

Since it landed, the rover has been moving along an irregular path (Fig. 1, Fig. Sup. S4), segmented by many stops and turnarounds points. The initial studies focused on the first hundreds of meters of the path by applying different analysis, processing, and inversion algorithms (Giannakis et al., 2021; Wang et al., 2021; Zhou et al., 2021) before data interpretation (Dong et al., 2020; Lai et al., 2020; Li et al., 2020; Dong et al., 2021). These early studies revealed a horizontally layered subsurface with an almost constant regolith thickness of ~10–12 m and several ejecta layers just below it, as well as deeper basalt layers (Lai et al., 2020; Li et al., 2020).

As the mission progressed, new LPR data was released, and new evidence of buried structures emerged from the data, such as a paleo-crater from a meteorite impact (Zhang et al., 2021a), dipping features (Feng et al., 2022), a "sandwich structure" within a paleo-crater (Zhou et al., 2022a), and crater-induced small faults (Chen et al., 2022).

Up to now, most of the studies used visual interpretation to detect horizons by only considering the reflection amplitude, while just in two

* Corresponding author.
E-mail address: groncoroni@units.it (G. Roncoroni).

https://doi.org/10.1016/j.icarus.2024.116219
Received 25 March 2024; Received in revised form 2 July 2024; Accepted 15 July 2024
Available online 18 July 2024

cases, single and basic signal attributes such as the instantaneous amplitude (Zhou et al., 2022b) and signal central frequency (Ding et al., 2020; Xu et al., 2020; Giannakis et al., 2024) were exploited. In this way, an unavoidable subjectivity was introduced into the interpretation process, and other analyses were additionally needed to support the interpretation, in particular numerical simulation and velocity analysis (Li et al., 2020; Giannakis et al., 2021; Wang et al., 2021; Zhou et al., 2022a; Chen et al., 2022). Diffraction hyperbolas analysis can be effective in estimating the electro-magnetic (EM) velocity field, from which properties such as dielectric permittivity and mean density can be further derived. However, there are intrinsic problems in addition to the limited number of diffractions (most of them concentrated in the shallower part of the profile, Fig. 2), their interference, and their often-irregular shape. A noteworthy issue is related to the not-rectilinear travel path of the rover on the Moon's surface which features abrupt changes of direction along a highly irregular route (Forte et al., 2023). In addition, there are some duplications mimicking hyperbolic patterns (Figs. Sup. S8, S10–S13), while they are actually due to backward sub-parallel paths of the rover (Fig. Sup. S9). Other studies estimated the dielectric constant from the reflection amplitude (e.g. Dong et al., 2020; Feng et al., 2023).

The low-frequency data of the LPR system is affected by interference phenomena first described for the CE-3 mission (Li et al., 2018) and then reported also for the CE-4 one (Pettinelli et al., 2021). The debate is still open (Zhang et al., 2021b) and some recent studies continued to exploit the low frequency dataset (Cao et al., 2023; Feng et al., 2023). However, our work focuses on the high-frequency LPR dataset thanks to its high quality and potential information content emerged from the previous analyses.

While in reflection seismics, several automatic or semi-automatic methods have been developed and nowadays are routinely applied for reflections tracking and assisting in data interpretation (e.g. Dorn, 1998), they are only seldom considered for GPR datasets (e.g. Dossi et al., 2015; Zhu et al., 2021). Similarly, while recently machine learning (ML) and neural network (NN) algorithms have been successfully applied for seismic data tracking (e.g. Di et al., 2020; Yang and Sun, 2019) demonstrating their powerful and effectiveness, they have not yet been fully exploited for GPR data. An exception is Roncoroni et al., 2022a in which a test of application was specifically dedicated to a GPR profile as well as Dinanta et al., 2022, and Liu et al., 2023 where NN techniques are used for specific target-detection purposes. In the latter paper, a detailed discussion about the advantages of such an approach can be found.

We therefore at first addressed the problem of reflectors extraction by applying a new automated method based on Deep Learning (DL) techniques, which provides objective and reliable results and has proven its effectiveness in different environments, datasets, and signal-to-noise ratios (Roncoroni et al., 2022a), (Fig. 2B, B′).

Then we exploited a combination of signal attributes that have already been successfully applied on GPR datasets (Sénéchal et al., 2000; Forte et al., 2012; Zhao et al., 2018) to further constrain and improve data interpretation.

For the first time, we here show the high-frequency LPR (CH-2) data recorded until 27th March 2023, representing the longest dataset (~1440 m) openly available at the time of writing, adding >400 m to the longest high frequency profile published so far presented in Giannakis et al., 2024. We show new structures previously not considered or imaged, while summarizing or partially re-interpreting the ones already described.

1.1. Overview of the CE-4 landing site and the geological context

The entire CE-4 landing zone, i.e. Von Kármán crater in the South-Pole Aitken basin region, exhibits a superposition of complex impact morphologies spanning from the pre-Nectarian to Copernican epochs. The oldest structure is the SPA basin, interpreted as one of the oldest, if not the oldest recognizable lunar basin (~4.3 Ga, Fernandes et al., 2013; White et al., 2020). The Von Kármán crater was predominantly dated as pre-Nectarian, i.e. ~4.2 Ga (Lu et al., 2021) though other references describe it as Nectarian (~4 Ga) (Feng et al., 2022). The neighboring impacts, notably Finsen, Alder, Leibniz, Maksutov, and Von Kármán L and L' (Fig. Sup. S1), produced ejecta materials that filled in and affected the bottom of the Von Kármán crater (Huang et al., 2018; Lu et al., 2021; Chang et al., 2021). The northern and eastern parts of Von Kármán are covered by ejecta from Lebnitz and Finsen craters, respectively, while in the western part mare basalts are up to the surface (Huang et al., 2018;

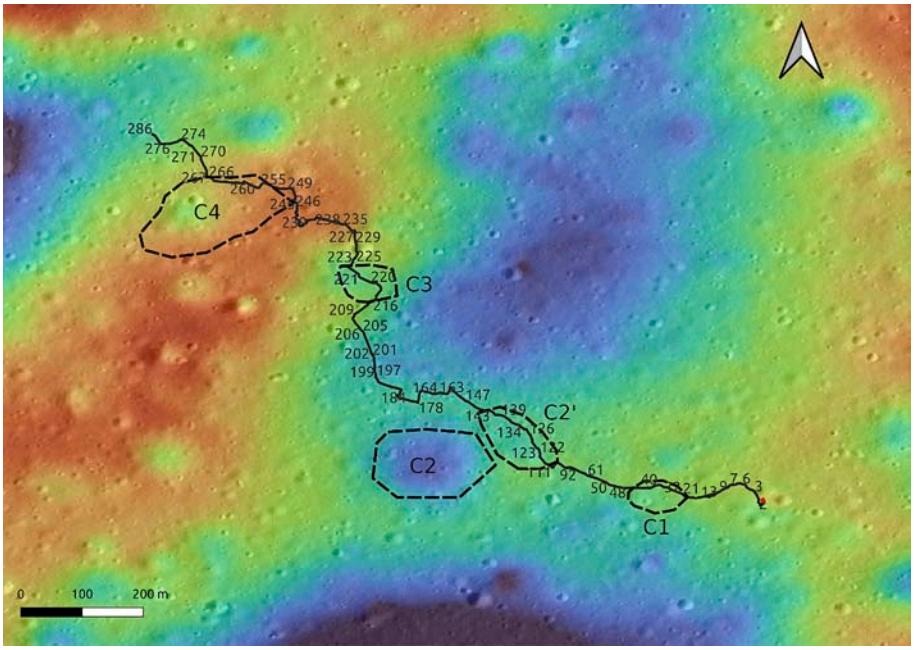

Fig. 1. Rover path with waypoint numbers superimposed on a fusion of topography and satellite image. C_n refer to craters and related structures described in the text. The red dot marks the landing point. Data from: https://quickmap.lroc.asu.edu/. (For interpretation of the references to colour in this figure legend, the reader is referred to the web version of this article.)

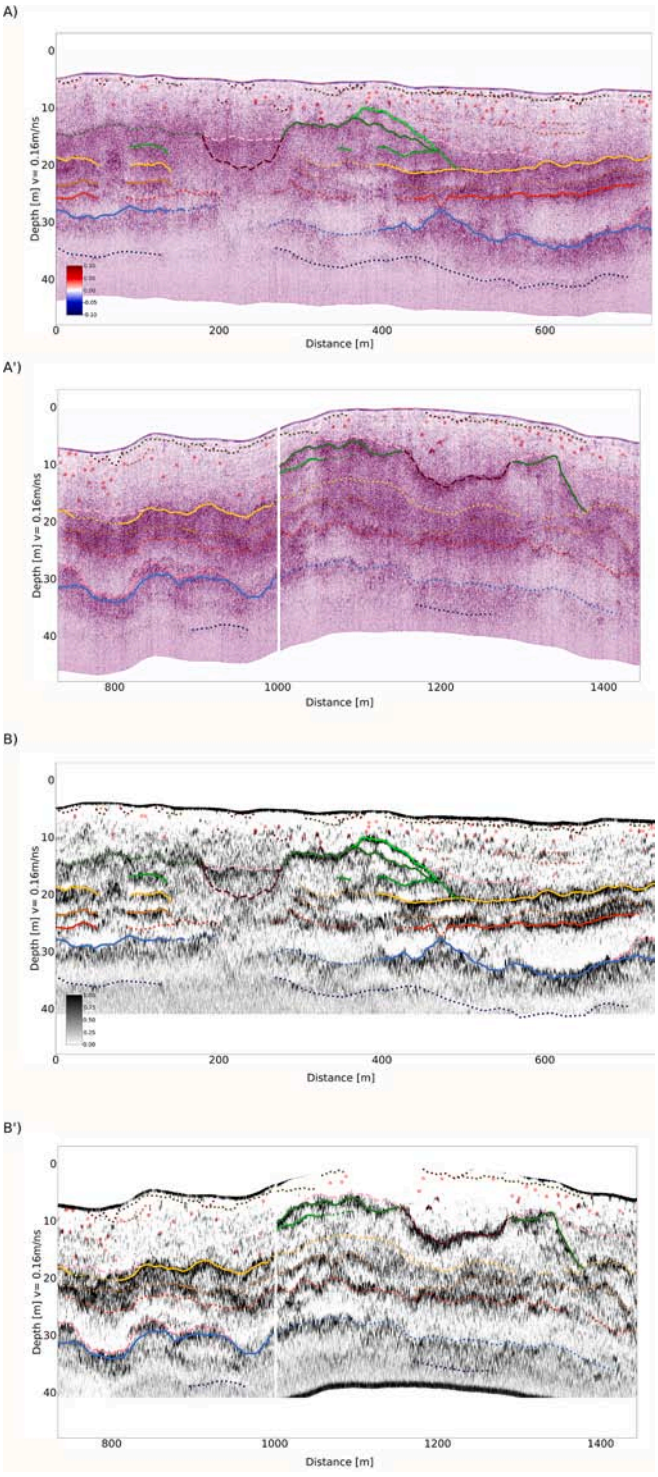

Fig. 2. Entire interpreted LPR dataset in normalized amplitude (A, A') and automated DL horizons extraction, in terms of reflections probability (B, B'). Light red dots represent localized scatterers, while continuous, dashed and dotted lines follow the main recognized reflectors. Each colour marks the same horizon in all the images. The data segmentation at about 1000 m is due to an about 20 m wide automatic duplicated traces removal (see Method section). (For interpretation of the references to colour in this figure legend, the reader is referred to the web version of this article.)

Lu et al., 2021) (Fig. Sup. S1, S2). The timing and relative sequence of these ejecta depositions and basalt flows are relevant for interpreting the local stratigraphy at the CE-4 landing site (Lai et al., 2020).

However, the studies up to date have shown a persistent inconsistency in the interpretation of the local stratigraphy (Chang et al., 2021). The Yutu-2 rover LPR profiles have been interpreted to show that the post-mare deposits at the CE-4 landing site are up to ~45 m thick, while a recent article (Giannakis et al., 2024) suggests a shallow basaltic lava layer starting at ~10 m depth. The Finsen crater has been unequivocally described as the dominant source of ejecta that covers the landing site (Huang et al., 2018; Lu et al., 2021; Xiao et al., 2021; Xu et al., 2021). Less agreement has been reached on the exact age of the Finsen crater, as it was reported to be either Eratosthenian (Fortezzo et al., 2020) (~3.0–3.1 Ga (Lu et al., 2021; Chang et al., 2021)) or Late Imbrian (~3.5 Ga (Gou et al., 2021) or ~ 3.6 Ga (Ivanov, 2018)). Further inconsistencies include the significance of the Alder crater (Imbrian (Lu et al., 2021) or Nectarian (Chang et al., 2021)) ejecta in the topmost (> 45 m) layer. While the interpretation of the early (and therefore shorter) Yutu-2 LPR data considered it a prominent component (Lai et al., 2020), subsequent studies found Alder crater ejecta to be negligible in the topmost layer, in agreement with remote sensing interpretations (Huang et al., 2018), and to possibly only occur beneath the youngest mare basalts at greater depths (>50 m (Lu et al., 2021; Chang et al., 2021; Xu et al., 2021)). Most recently, four craters have been identified as principal sources of primary ejecta at the CE-4 landing site, and their most likely emplacement sequence from older to younger (Xu et al., 2021) is: Maksutov, Von Kármán L′, Von Kármán L (all late-Imbrian), and then Finsen. The ejecta delivered by larger and older impacts like Leibnitz and Schrödinger, or as distant as Imbrium or Orientale, are expected at greater depth, not accessible by LPR CH-2, beneath mare basalts (Xiao et al., 2021). The mare basalts flooded the floor of the Von Kármán in several episodes, namely between ~3.15 and 3.75 Ga (Ling et al., 2019). Those deeper structures and stratigraphy, for instance, the oldest basalt flows, that occur at depths greater than ~50 m have been assessed using the lower-frequency CH-1 (Lai et al., 2020; Cao et al., 2023). However, their reliability is still debated (Cao et al., 2023).

2. Methods

Radar data pre-processing is a crucial step before data analysis and interpretation of any subsurface structure. In addition to the normal processing flow, that is performed also on the Terrestrial GPR data, i.e. time-varying gain, zero-offset, bandpass filter, and background removal, we observed problems related to duplicated traces and data file stitching (Lai et al., 2021; Forte et al., 2023). Importantly, removal of redundant data is a critical step due to the acquisition system, since the rover stops to acquire other measurements like panoramic cam or visible near infrared spectra without interrupting the acquisition of LPR data. This process generates raw data with local redundancies that need to be removed. We have designed an algorithm capable of performing this removal automatically and minimizing the subjectivity of the procedure, saving time, and avoiding residual duplications (Fig. Sup. S13). The entire algorithm is available in Roncoroni et al., 2024.

Moreover, data acquired on different days is stored separately in different files (SOL) and needs to be merged to get a manageable full dataset. 634,419 A-scans (i.e. traces) for a total length of the path equal to ~1440 m within the SOL range (lunar days) between 01 (4th January 2019) and 286 (27th March 2023) have been released at the moment of writing (January 2024) and are downloadable at https://moon.bao.ac.cn/ce5web/moonGisMap.search (Table Sup. S1 provides the list of all the used original files). In Roncoroni et al., 2024 the entire LPR CH2 dataset is fully described and can be downloaded in both original and different edited and processed versions.

Beside standard processing steps, one of the commonly applied GPR processing algorithms is migration: its purpose is to correct for the distortions that can occur in the recorded signals due to both subsurface

dipping reflectors, and diffraction of the electromagnetic waves (scattering), see e.g. Jol, 2009.

The migration changes the reflectors dip, location and length only if they are not horizontal, while in the latter case they are not modified anymore (Yilmaz, 2001). Since for migration the EM velocity model is the most crucial parameter, we chose not to apply it due to the rover's non-linear path (Fig. Sup. S8, S9) and also because the out-of-plane hyperbolas (Jiao et al., 2000) did not allow for retrieval of a trustful velocity model. Such events are expected within the regolith, which is composed of heterogeneous materials with many possible lateral scatterers. On the other hand, the migration of the data can surely focus diffraction hyperbolas, but such a distinct hyperbolic shape can be exploited in localizing the scatterers. Therefore, the migration procedure would not allow us to retrieve better resolution and would potentially heavily degrade the imaging especially of deeper horizons, for which there are no reliable constraints on the velocity model, and signal degradation is expected due to border effects (Yilmaz, 2001).

For similar reasons, time-to-depth conversion was done using a constant EM velocity equal to 0.16 m/ns. It is certainly true that a more detailed velocity field could be reconstructed exploiting diffraction hyperbolas, but as previously pointed out, there are intrinsic limitations.

2.1. LPR horizon extraction

For the automatic horizon extraction (Fig. 2b and b') we modified the workflow proposed in Roncoroni et al., 2022a, 2022b, implementing and exploiting a NN that takes both the data amplitude and the cosine of the instantaneous phase, as inputs. The entire training model and codes can be found in https://github.com/Giacomo-Roncoroni/CE4-HrEx.

The algorithm uses a Long Short-Term Memory (LSTM) (Hochreiter and Schmidhuber, 1997) architecture to maintain the causality of the data and take advantage of its ability to better fit the physics behind wave propagation. The use of Bi-Directional LSTM is also employed to improve the accuracy of NN classification.

The training data generation for the LSTM is based on synthetic GPR traces created by convolving a wavelet with a reflectivity function and adding noise, Roncoroni et al., 2022a. This process allowed for the generation a hige ammount of synthetic data representing a wide range of conditions typically encountered in field datasets, ensuring the NN's robustness and adaptability to various signal and noise characteristics.

The output of the NN is driven by a dense layer with two neurons and a SoftMax activation function (Mannor et al., 2005) that outputs a probability value indicating the presence of reflections as a function of recording time. The methodology is fully 1-D, so it separately considers A-scans (i.e. single traces). Further details about the choice, implementation, and strength of the NN can be found in Roncoroni et al., 2022a.

We trained the NN using a synthetic GPR dataset composed of 100,000 traces (a.k.a. A-scans) to eliminate potential biases arising from the field dataset and to exert full control over the NN performance through the known subsurface model that generated the training data. The reference output was represented by a binary indicator (1,0) labeling each sample as either representing a signal reflection or not, respectively. Therefore, the first prediction output is given as a probability set, where each point is associated with a probability range indicating its likelihood of belonging to a reflector. Then, to obtain the binary indicator we just set a threshold, estimated by evaluating the number of points classified as reflectors at various threshold values, and selecting the sharp inflection point in the resulting curve. This method minimizes the subjectivity of the choice and is applied as a constant on the entire dataset.

Since we are working with a 1-D methodology, to reduce the noise effect we trained the NN to predict the whole wave package and not only its maximum phase, as performed in Roncoroni et al., 2022a. To mitigate the uncertainty in predictions, an ensemble learning strategy was employed. This strategy leverages multiple learning algorithms to achieve improved predictive outcomes (Mendes-Moreira et al., 2009). This methodology resulted in two separate predictions, which were then combined using their geometric mean, as it provided better results compared to the arithmetic mean. This can be attributed to the nature of the prediction, where probabilities in the range [0–1] are being predicted, as plotted in Fig. 2b and b'. Null values represent no horizon probability, while values equal to 1 the maximum probability.

2.2. LPR attributes analysis

Attribute analysis is a technique used to extract features and information from GPR data to support interpretation and data analysis and at first exploited for reflection seismic data (Chopra and Marfurt, 2007). In this paper we used several attributes to get a more detailed and constrained LPR interpretation and to verify and validate the results obtained with the automated horizon extraction. In particular, we calculated:

- *Cosine of the instantaneous phase* (Chopra et Marfurt, 2007) (a.k.a. cosine of phase): it is a complex and amplitude independent attribute that clearly displays bedding (Fig. Sup. S16 and details in Fig. 7).
- *Dominant Frequency* (Chopra and Marfurt, 2007) it is a complex attribute, commonly used for highlighting specific events, such as abnormal attenuation and thin bed tuning (Fig. Sup. S18, S19, S20).
- *Sweetness* (Oliveros and Radovich, 1997): It is an attribute computed by dividing the trace envelope by the square root of the instantaneous frequency (Fig. Sup. S17, S19, S20). It is able to characterize and emphasize differences between various facies.

3. Results

3.1. Analysis of the topography of the CE-4 landing site

The topography of the terrain where the rover landed is dominated by sub-parallel ejecta rays interpreted to originate mainly from the Finsen crater (Fig. Sup. S3). This is reflected in the distribution of alternating ~400–500 m wide topographic low and high zones, occasionally connected by lower-lying bridging material (Fig. 1, Fig. Sup. S5). The rover has landed on a relatively high zone and the first 400 m of the path covered these ejecta-rich strata. The path then continues across a lower zone ~500 m wide that is followed by another high zone ~1000–1300 m along the path (Fig. 1). The final ~100 m of the path, undisclosed until now, is placed toward another low zone. This topography seems to play an essential role in ejecta distribution, but earlier studies have not fully considered it.

3.2. LPR profile interpretation and stratigraphy

We describe different stratigraphic units interpreted by exploiting LPR data of the ~1440 m long rover path, focusing on the first ~50 m depth. The rover path is presented in Fig. 1 (the landing site is marked by the red dot), and the radar profile in Fig. 2 (the landing site is on the left side). In discussing the results, we outline the stratigraphy as obtained by automated NN extraction, integrated by radar attributes evaluation (see Methods).

The DL horizon extraction (Fig. 2b) highlights some reflectors which are almost continuous along the entire profile, as well as other horizons present only in specific locations. By integrating the reflector probability (Fig. 2b) with the reflection amplitude (Fig. 2a) and combining multi attribute analysis (Fig. 3; Fig. Sup. S15-S20), we can interpret single horizons, their spatial correlation and facies: similar colors represent the same stratigraphic level along the radar profile (Fig. 2b, c; Fig. 3).

Moreover, we interpreted beneath the entire rover path different EM units (U1–U4) on the basis of their EM signature, geometry and relative location, as detailed below (Fig. 4).

U1 has a low overall reflectivity, without clear and coherent high

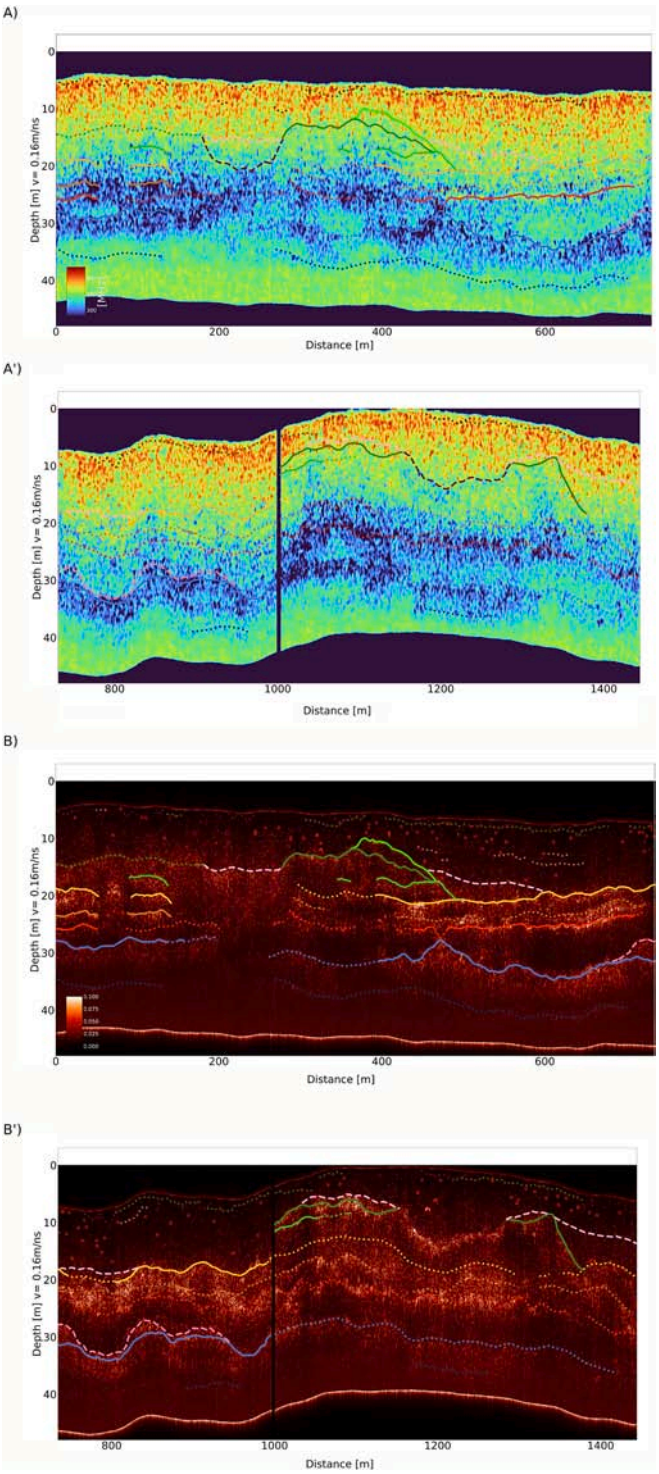

Fig. 3. Entire interpreted LPR dataset: smoothed dominant frequency (A, A'); sweetness (B, B'). Light red dots represent localized scatterers, while continuous, dashed and dotted lines follow the main recognized reflectors. Each colour marks the same horizon in all the images, as in Fig. 2. (For interpretation of the references to colour in this figure legend, the reader is referred to the web version of this article.)

amplitude reflections. This unit can be observed from the topographic surface down to an almost constant depth of ~12 m, seen from the landing site position to a distance of 275 m, decreasing down to as low as 6 m at a distance of 380 m and then approaching 15 m between 500 and 950 m (Fig. 4). Its thickness is again lower (5–10 m) until 1350 m, then it increases again at the end of the profile. Within U1 we imaged two new types of structures: at least 20 have a concave shape, while several others are characterized by local sub-horizontal reflectors. None of these features have been previously reported, probably because they have an overall low signal amplitude, but appear very clear when phase or other composite attributes like *sweetness* (see Methods) are considered (Fig. 3, S17). The concave structures appear close to the surface and have a mean width equal to 16.4 m (maximum 23.2 m; minimum 8.3 m) and some of them are partially overlapping. We interpret all those structures as filled craters produced by either small meteorites or, most likely, as secondary craters that are very frequent in this area. Some of these craters appear concealed at the top with a quite discontinuous but still recognizable sub-horizontal reflector (e.g. at 1220 m, Fig. Sup. S20). In addition to these reflectors, some other deeper and significantly longer ones have been imaged within U1 and specifically between 450 and 780 m. They show a maximum (apparent) dip equal to 6° between 450 and 500 m where they lie over dipping layers of U2. The maximum lateral extension of a single reflector reaches 70 m, demonstrating that the regolith is, at least locally, layered and shows some stratifications that follow the former (i.e. deeper) morphology.

Stronger reflectors are present beneath ~12 m depth from the top of the profile, including discrete horizontal and slightly dipping reflectors down to a depth of ~30 m. These layered zones can be classified into two separate stratigraphic units based on their amplitude, signature and lateral continuity (Fig. Sup. S16-S18): the upper one (U2) that is ~8–10 m thick and entails two roughly equally thick layers (green in Figs. 2 and 4), and the slightly thicker beneath (~12 m, U3) that contains up to three layers (orange to red in Fig. 2, light blue in Fig. 4).

U2 is present in the first 480 m of the profile and from ~950 to 1350 m, while U3 can be observed throughout the profile. At a depth of ~30 m, a strong reflector appears (with local lower reflectivity) with significantly different characteristics from those of the facies above (see e.g. Fig. Sup. S18), and persists laterally throughout the observed profile (U4 in Fig. 4).

The actual stratigraphy is also determined by the excavated local materials mixed with that ejecta and reworked by multiple impacts. The final stratigraphic layers rather reflect the mixture of the primary ejecta and the excavated local materials (i.e. ejecta deposits) (Xu et al., 2021) and the thicknesses of the U1–U4 layers described here are broadly in agreement with previously interpreted thicknesses. In this regard, U1 has been interpreted as fine-grained regolith (e.g. Li et al., 2020; Lai et al., 2020; Zhang et al., 2021a; Chen et al., 2022) dominated by Finsen ejecta which was then reworked, mixed and overturned by numerous impacts but compositionally it is very similar to the ejecta itself (Lin et al., 2020; Dong et al., 2021; Guo et al., 2021). In addition to several low amplitude interfering events, made clear by phase analysis (see e.g. Fig. Sup. S16), there are some localized scatterers having different amplitudes, alternatively interpreted as decimeter-sized boulders ejected during the formation of Finsen crater, including an unknown fraction of local rocks (Chen et al., 2022), or as broken pieces of glass-bearing breccia projectiles excavated from pre-existing small craters on the lunar farside (Lin et al., 2020). Some authors further divide U1 into two sub-units: the topmost is more homogeneous with weaker amplitude because the surface materials have undergone a longer weathering period, while the lower portion has a high overall reflectivity interpreted as a less weathered material (Zhang et al., 2020). This division is not apparent in our analysis, even if the shallower part of U1 seems to have higher numbers of scatterers than the deeper one.

Discrete layers within U2 and U3 (~12–30 m deep) correspond to what has been previously described as different coarse ejecta deposits i.e. the mixture zone of Finsen's primary ejecta, pre-Finsen primary ejecta (Maksutov, Von Kármán L′, and Von Kármán L) and local basalt materials (Xu et al., 2021).

The lowest U4 most probably represents a mare basalt layer >30 m deep, as already pointed out by several studies (e.g. Guo et al., 2021; Zhang et al., 2021a), with some discontinuous highly attenuated

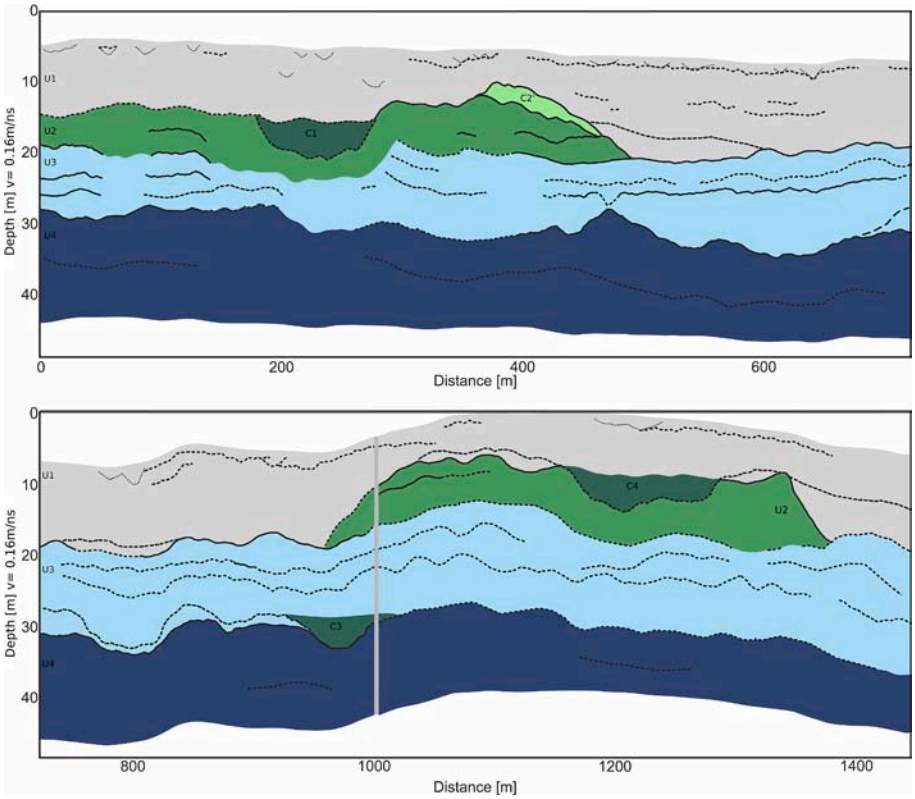

Fig. 4. Subsurface units assessment from LPR data interpretation (Figs. 2, 3). U1 (grey), U2 (green), U3 (light blue), U4 (blue) represent different macro units. C1, C2', C3 and C4 are interpreted as paleo-crater filling materials, while dotted and dashed lines mark layering and peculiar structures within the main units (see text for description and details). (For interpretation of the references to colour in this figure legend, the reader is referred to the web version of this article.)

internal layers also due to low overall signal-to-noise ratio of LPR high frequency data for high depth. This seems to be confirmed by the signal frequency behavior (Fig. 3) even if a recent paper (Giannakis et al., 2024) suggests a different interpretation. However, a conclusive interpretation of such a unit is not possible just from the analysis of LPR data.

In general, the observed stratigraphy is quite in agreement with strata described earlier (Xu et al., 2021; Zhang et al., 2021a; Lai et al., 2021). However, notable discrepancies and new imaged structures will be discussed especially regarding U1, U2 and paleo craters structures C1 to C4.

4. Discussion

The CE-4 landing site shows a morphology with alternating topographic lows and highs reflecting Finsen ejecta rays, which are transected by the Yutu-2 rover (Figs. 1, 5). In particular, based on a fine-scale digital terrain model (DTM) map we detected four crater shapes (C1 to C4 in Fig. 1) crossed by, or very close to the rover path. Crater C1 is buried just below the regolith and developed within U2. It was first interpreted by Zhou et al., 2021 and then confirmed by several other authors. We estimated its maximal excavation depth (d) as a function of the crater diameter (D) using the relation d = 0. 084D (Melosh, 1989; Warner et al., 2017) (Fig. 4). Marco Figuera et al., 2022 proposed for the Moon different relations for craters with or without permanent shadowed regions, which are not applicable in our study. However, also considering the intrinsic errors due to approximations done for both vertical and lateral LPR velocities, here we just want to consider an order of magnitude value.

For C1, exploiting the above reported relation, we obtained a depth of 8.8 m, being D = 105 m, which is in good agreement with the interpreted paleo crater which extends to a maximum depth based on the LPR data of 8.0 m. If we consider the entire zone in which the

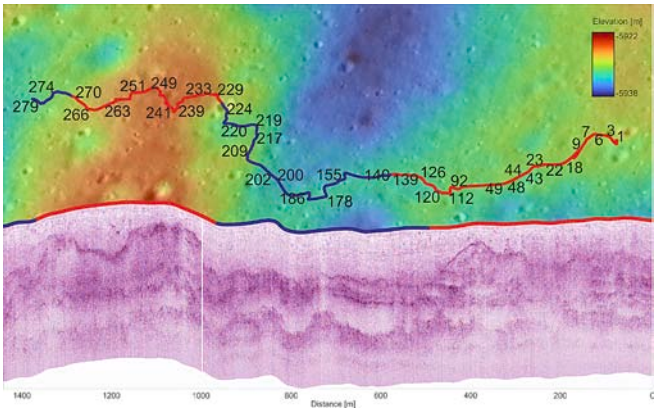

Fig. 5. Correlation of surface and sub-surface structures. Plain view of the rover path and correlation with LPR processed profile (in amplitude). Red and blue segments highlight high and low topography zones, respectively. Landing point is at location 1. Data from: https://quickmap.lroc.asu.edu/. (For interpretation of the references to colour in this figure legend, the reader is referred to the web version of this article.)

layering is absent as the crater diameter, having an extension at its top of about 125 m, an excavation depth of 10.5 m is obtained: it matches the vertical extension in which the layers are absent i.e., from the pink dashed line (top of the crater filling materials) down to the brown dashed line (Fig. 2).

C3 crater is quite clear on the surface morphology which can be related to the interpreted location of the crater on LPR data, however its filling and its actual geometry are not easy to be defined.

The same geometrical analysis was performed on C4, which has a

diameter equal to about 142 m and an estimated excavation depth from LPR data of 6 m. By applying the previously reported relation, we obtain a d value equal to 11.9 m, which does not match the actual geometry of C4, possibly because this crater was modified after the main impact, as suggested also by its very irregular shape.

A similar analysis performed on the 20 shallow craters (some of them being coalescent), (Fig. 2) gives a mean diameter of 16.4 m and a consequent excavation depth of 1.4 m. Even in this case, such a value is quite similar to the depth imaged by the LPR data, which values range from 0.9 to 2.4 m. The similar size and their close and regular spatial distribution suggest they were created as secondary craters.

A peculiar structure is labeled as C2' in Figs. 1 and 4. It lies on the top of U2 between 360 and 460 m on the profile. In this portion, LPR path crosses the rim of crater C2 whose center is to the south of the profile. C2 is an elliptical crater ~145 m (North-South) by ~195 m (East-West) wide and evident on the surface morphology; it is not visible on the LPR profile since it develops outside from the investigated area (see Fig. 1), but another craterform structure (C2') is apparent.

This smaller (max wideness in NW-SE direction equal to about 115 m) and younger crater C2' (Fig. 6) superimposed on the rim of the main crater C2 (estimated to be younger than 100 Ma (Lai et al., 2021)) appears quite fresh. In particular, it is apparent when considering the surface azimuth (Fig. 6c), while on the surface slope image (Fig. 6d) it is quite smooth. On the satellite imagery (Fig. 6a) this structure is not recognizable, while on the surface elevation (Fig. 6b) it is not very evident. The very high reflectivity and reflection continuity of the corresponding LPR horizon (marked in light green in Fig. 2) imply that it entails, at least partially, possible impact melt that was created on the rim of C2.

DL driven interpretation of the LPR data, integrated with attribute analysis and satellite imagery, allowed to extract the stratigraphic horizons, correlate them spatially, and group the main units, instead of using a more subjective manual line drawing interpretation. While the overall structure revealed by this method agrees reasonably well with previous observations (e.g. Lai et al., 2021; Zhang et al., 2021b; Chen et al., 2022; Feng et al., 2022, it allows, for the first time, the recognition of novel and less evident sub-surface structures. Importantly, using this integrated interpretation, we were able to distinguish stratigraphic units with different electromagnetic characteristics, and not only generic "reflectors", as well as to recognize their correlation with the present-day topography. The level of detail in the interpretation is enhanced compared to previous studies, as well as its objectivity. For instance, we found that U2 is not present in the central part of the LPR profile (480–950 m). Notably, based on topography and distribution of lows and highs, it can be observed that this segment of missing U2 unit corresponds to the lower terrain (Fig. 5). Based on this observation, we suggest that the U2 unit, whose top is the first strong layered reflector beneath the regolith, corresponds to the top of the Finsen ejecta. At the end of the LPR profile, U2 is no longer present since the path is approaching another low topographic area, in which Finsen ejecta is not expected (Fig. 1, Fig. 5). Therefore, the U2 layer can be identified as directly deposited by the Finsen event. On the other hand, our integrated LPR data analysis and horizon extraction do not confirm the faults suggested by Chen et al., 2022. We found local interruptions of some reflectors and the previously described peculiar lack of reflectors close to the buried crater C1, but no fault-like features.

All available studies consider a homogeneous regolith without clear internal reflectors, only with local high amplitude scatterers with the exception of Giannakis et al., 2021 and 2024, which did not directly recognize layering within the regolith, but evidenced lateral and vertical macro electrical permittivity changes within it. Such Authors implemented and applied a method to estimate the electrical permittivity exploiting a new approach for diffraction hyperbolas fitting, but limited to the shallower 150 ns (i.e. 12 m considering a constant EM velocity equal to 0.16 m/ns) of CE-4 LPR data. We here show not only that the layering is visible and clearly imaged on the radar profile, but that it is

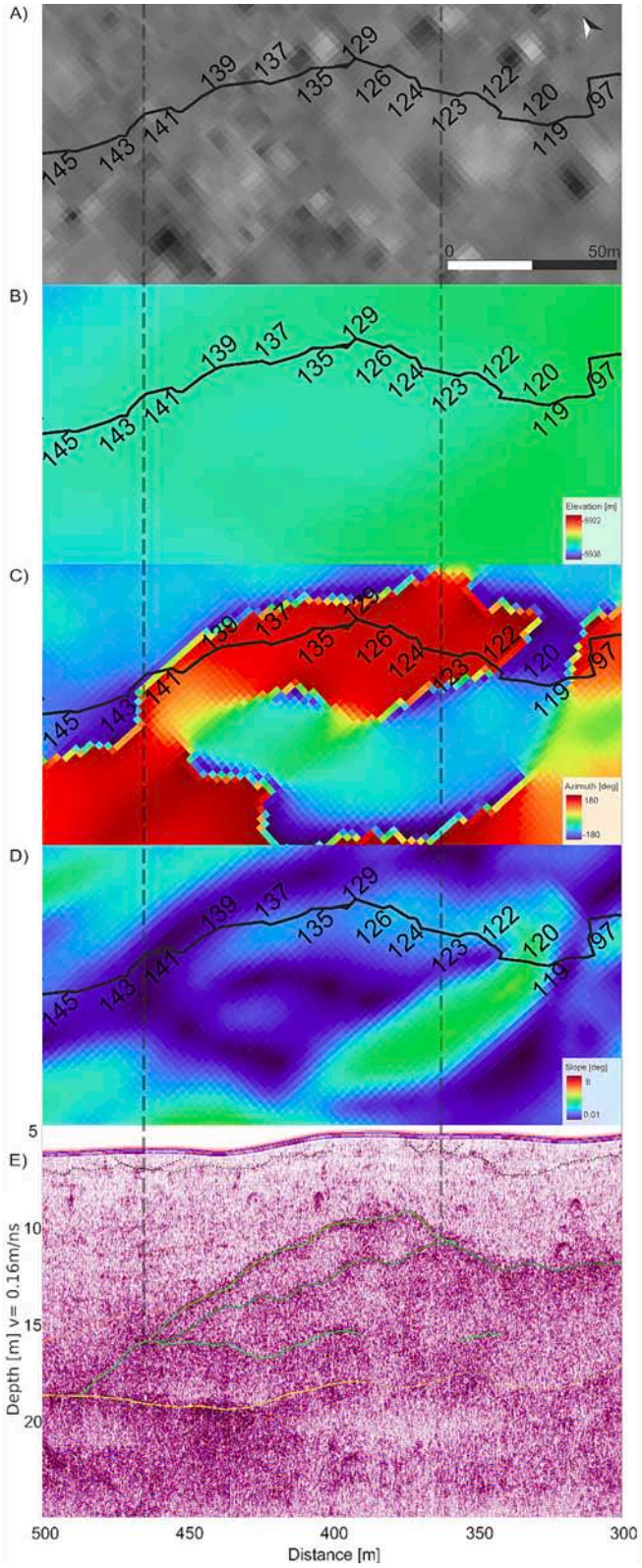

Fig. 6. Analysis of the LPR portion between SOL 95 and 145 and comparison with surface morphology. A) Satellite photograph; B) surface elevation; C) terrain aspect; D) terrain slope; E) LPR interpreted data.

slightly dipping and follows the deeper paleo-topography. This observation is an independent support toward the fact that the Finsen ejecta were deposited in alternating lows and highs which formed a paleo-topography of the terrain as early as ~3 Ga ago, or even earlier. The regolith layers were then deposited following this paleo-relief and were not entirely annihilated by the subsequent impacts. As layers do not show complete homogeneous mixing, it is expected that the Finsen ejecta would not completely mix with ejecta from previous craters and the layers dominated by previous ejecta may still exist. However, most likely the topmost layer is a mixture of dominantly Finsen ejecta with pre-materials, in agreement with the geological mapping, suggesting dominance of the Finsen ejecta in this entire portion of the Von Kármán crater, crossed by SW-NE ejecta rays from Finsen and dominated by characteristic orthopyroxene (Huang et al., 2018) (Fig. Sup. S3).

It is interesting to notice that, in agreement with the analysis recently proposed by Giannakis et al., 2024 (see the central frequency and its smoothed version in fig. 9 therein), the dominant frequency attribute (Fig. 3a, a' and Sup. S18–S20) has a peculiar trend. In fact, it decreases for increasing depths, as expected due to the well-known low pass filtering effect due to the materials (e.g. Neto and Medeiros, 2006), but with a significantly different lateral behavior. In particular: U1 is always characterized by the highest frequency content, gradually decreasing with depth; U2 (and C1, C2', C3, C4) exhibit intermediate frequencies; U3 has a lower dominant frequency (blue colors in Fig. 3a, a'); U4 is characterized by an intermediate frequency content. The latter is probably related to the lower signal-to-noise ratio close to the bottom of the record, but all the other features seem to be realistic. In particular, there is a significantly different spectral signature between C3 (characterized by intermediate frequencies) and its surroundings where low frequencies dominate, further confirming that C3 is most probably a filled paleo crater.

In addition to regolith internal layering, for the first time, at least 20

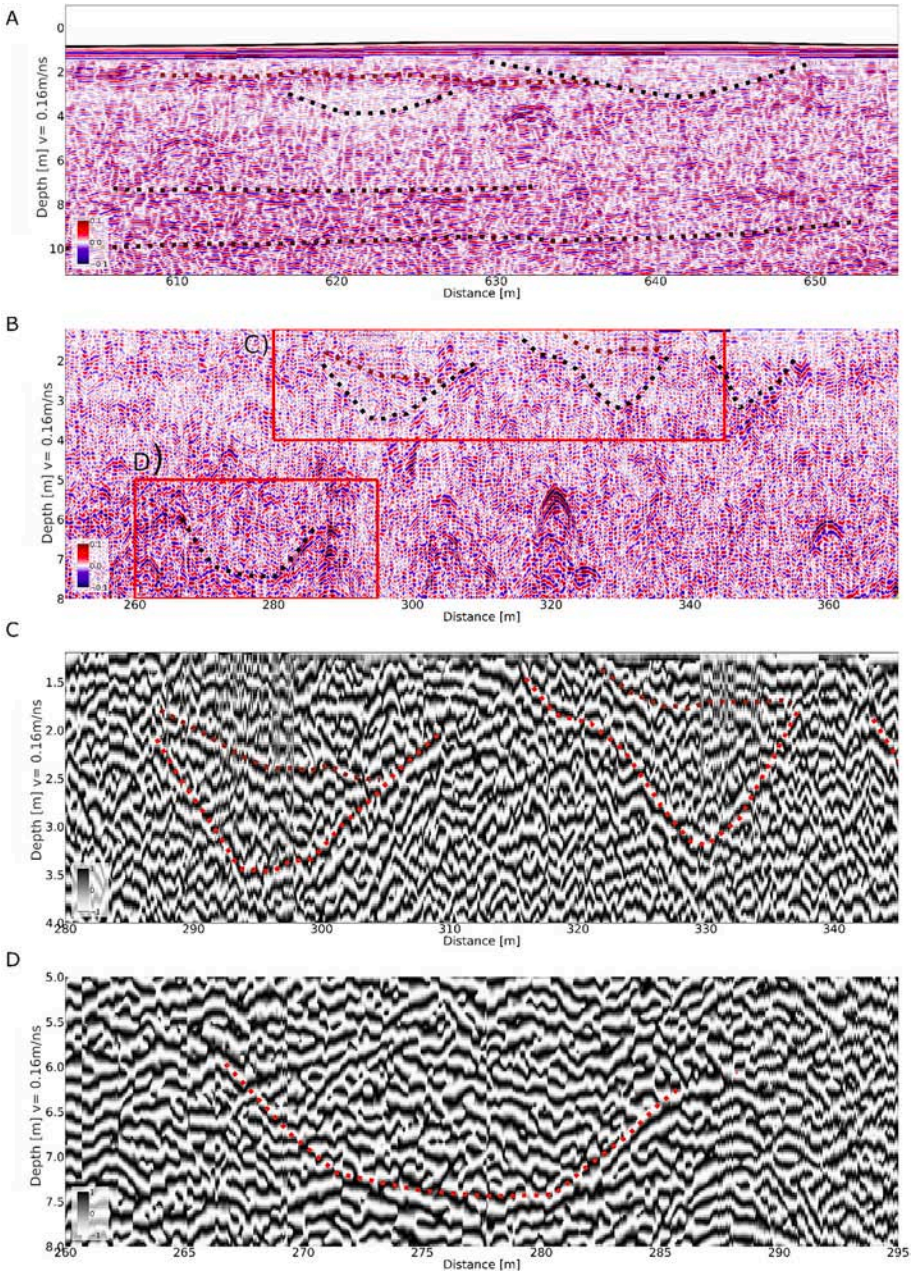

Fig. 7. Details of layering and shallow craterform structures within the regolith (U1), A) and B). C) and D) show the cosine of instantaneous phase calculated within red boxes in B). (For interpretation of the references to colour in this figure legend, the reader is referred to the web version of this article.)

shallow buried craterforms have been detected on the LPR dataset. They are not apparent on the base of LPR reflection amplitude (Fig. 7) suggesting, as expected, that the filling material is very similar to the surrounding one. However, using signal attributes and in particular phase attributes (Fig. 7) the lateral limit of such craters is evident and can be quite easily imaged even when the DL horizon extraction does not clearly recognize any apparent structures.

5. Conclusions

New accessible LPR data and DL-based interpretation allowed us to identify new subsurface structures on the farside of the Moon. In particular, while available studies detected a homogeneous regolith with only local scatterers and no apparent reflectors, we not only show that several layers can be imaged exploiting the LPR data, but also that they are not always horizontal but rather follow the deeper paleo-topography. The DL automated horizon probability procedure integrated with the analysis of combined signal attributes, allowed the discovery of fine-scale features in regolith and ejecta layers which were not previously imaged, probably due to their low overall amplitude and elusive nature. In particular, we recognized at least twenty shallow buried crater-like structures within the regolith and further four developed deeper within different stratigraphic units. We made a relevant step forward in correlating layers and defining their different geological meaning. The LPR dataset was not interpreted as a stand-alone information, but it was fully integrated with satellite-derived information, and specifically to surface photographs and detailed elevation models, finding that some subsurface units are well correlated with the present-day topography. This observation is an independent support toward the fact that the Finsen ejecta was deposited in alternating lows and highs which formed a paleo-topography of the terrain. Thanks to the exploited integrated data approach, we assigned specific geological and geomorphological meaning to the identified subsurface reflectors, defining four different main units along the considered rover path, and describing their relationship. The obtained results proved the importance of integrated analysis of lunar data for subsurface assessment and structure identification, which are in turn crucial for possible resources evaluation. Further research will be addressed to the calculation of DL-based attributes analysis.

In the future, the machine learning algorithm as proposed in this paper could be used for the lunar rover to automatically extract subsurface target information such as the layered structure, lava tube, crater and rock body, so as to provide information support for the rover to independently plan its route path and obtain more valuable scientific data.

CRediT authorship contribution statement

G. Roncoroni: Writing – review & editing, Writing – original draft, Visualization, Software, Resources, Methodology, Investigation, Data curation, Conceptualization. **E. Forte:** Writing – review & editing, Writing – original draft, Supervision, Methodology, Data curation, Conceptualization. **I. Santin:** Writing – review & editing, Writing – original draft, Visualization, Validation, Methodology, Conceptualization. **A. Černok:** Writing – review & editing. **A. Rajšić:** Writing – review & editing. **A. Frigeri:** Writing – review & editing. **W. Zhao:** Writing – review & editing. **G. Fang:** Supervision. **M. Pipan:** Writing – review & editing, Supervision, Resources, Project administration, Funding acquisition, Formal analysis, Conceptualization.

Declaration of competing interest

The authors declare that they have no known competing financial interests or personal relationships that could have appeared to influence the work reported in this paper.

Open research

Data can be found on 2019 DOI: https://dx.doi.org/10.12350/CLPDS.GRAS.CE4.LPR-2B-2019.vA [Dataset] and 2020 DOI: https://dx.doi.org/10.12350/CLPDS.GRAS.CE4.LPR-2B-2020.vA [Dataset]. Ground Research and Application System of China's Lunar and Planetary Exploration Program. Chang'E-4 Lunar Penetrating Radar Level 2B scientific Dataset. China National Space Administration, 2020.

The full LPR CH4 dataset can be found in different versions and formats in Roncoroni et al., 2024.

The codes related to the horizon extraction algorithm can be found at https://github.com/Giacomo-Roncoroni/CE4-HrEx [Software], while the codes for data pre-processing at https://doi.org/10.6084/m9.figshare.23798466.v1 [Codes]. Processed data is available at https://doi.org/10.6084/m9.figshare.23723922.v1 [Dataset, SEG-Y format], and at https://doi.org/10.6084/m9.figshare.23723976.v1 [Dataset, PDS4 format].

Acknowledgments

We thank the Chang'E-4 payload team for mission operations and China National Space Administration for providing the Chang'E-4 data that made this study possible. This work was supported by the National Natural Science Foundation of China (11773023, 11941001, U1631124) and the Civil Aerospace Pre-research Project (D020302). The Chang'E-4 data used in this work is processed and produced by "Ground Research and Application System (GRAS) of China's Lunar and Planetary Exploration Program, it can be downloaded at http://moon.bao.ac.cn/ce5web/searchOrder_dataSearchData.search.

A. Č. acknowledges Rita Levi Montalcini fellowship by the Italian Ministry of University and Research (MUR).

G. R. acknowledges the IG of the PNRR spoke 2, National Centre for HPC, Big Data and Quantum Computing (J93C22000540006): "Blending Machine Learning with advanced numerical simulations: application to the sustainable exploitation of natural resources".

We would like to thank the editor prof. B. Johnson and two anonymous reviewers for their advisable comments and suggestions.

Appendix A. Supplementary data

Supplementary data to this article can be found online at https://doi.org/10.1016/j.icarus.2024.116219.

References

Byrne, C.J., 2008. The south pole-Aitken Basin and the south polar region. In: Byrne, C.J. (Ed.), The Far Side of the Moon: A Photographic Guide. Springer, New York, pp. 60–93. https://doi.org/10.1007/978-0-387-73206-0_8.

Cao, H., Xu, Y., Xu, L., Zhang, L., Bugiolacchi, R., Zhang, F., 2023. From Schrodinger to Von Kármán: an intriguing new geological structure revealed by the Chang'e-4 Lunar Penetrating Radar. Geophys. Res. Lett. 50 (2) https://doi.org/10.1029/2022GL101413 e2022GL101413.

Chang, Y., Xiao, Z., Wang, Y., Ding, C., Cui, J., Cai, Y., 2021. An updated constraint on the local stratigraphy at the Chang'E-4 landing site. Earth Planet. Phys. 5 (1) https://doi.org/10.26464/epp2021007 eepp2021007.

Chen, R., Xu, Y., Xie, M., Zhang, L., Niu, S., Bugiolacchi, R., 2022. Sub-surface stratification and dielectric permittivity distribution at the Chang'E-4 landing site revealed by the lunar penetrating radar. Astron. Astrophys. 664, A35. https://doi.org/10.1051/0004-6361/202142677.

Chopra, S., Marfurt, K.J., 2007. Seismic Attributes for Prospect Identification and Reservoir Characterization (Society of Exploration Geophysicists and European Association of Geoscientists and Engineers, 2007). https://doi.org/10.1190/1.9781560801900.

Di, H., Li, Z., Maniar, H., Abubakar, A., 2020. Seismic stratigraphy interpretation by deep convolutional neural networks: a supervised workflow. Geophysics 85 (40), WA77–WA86. https://doi.org/10.1190/geo2019-0433.1.

Dinanta, G.P., Fernando, D., Setyaningrum, N., Meliani, F., Widodo, J., Setiyoko, A., et al., 2022. Deep learning for ground penetration radar reflection images in civil structures investigation. In: IEEE International Conference on Aerospace Electronics and Remote Sensing Technology (ICARES), Yogyakarta, Indonesia, pp. 1–7. https://doi.org/10.1109/ICARES56907.2022.9993511.

Ding, C., Xiao, Z., Su, Y., Zhao, J., Cui, J., 2020. Compositional variations along the route of Chang'e-3 Yutu rover revealed by the lunar penetrating radar. Prog. Earth Planet. Sci. 7 (32) https://doi.org/10.1186/s40645-020-00340-4.
Dong, Z., Fang, G., Zhao, D., Zhou, B., Gao, Y., Ji, Y., 2020. Dielectric properties of lunar subsurface materials. Geophys. Res. Lett. 47 (22) https://doi.org/10.1029/2020GL089264 e2020GL089264.
Dong, Z., Fang, G., Zhou, B., Zhao, D., Gao, Y., Ji, Y., 2021. Properties of lunar regolith on the Moon's farside unveiled by Chang'E-4 Lunar Penetrating Radar. J. Geophys. Res. Planets 126 (6). https://doi.org/10.1029/2020JE006564 e2020JE006564.
Dorn, G.A., 1998. Modern 3-D seismic interpretation. Lead. Edge 17 (9), 1262–1269.
Dossi, M., Forte, E., Pipan, M., 2015. Automated reflection picking and polarity assessment through attribute analysis: theory and application to synthetic and real ground-penetrating radar data. Geophysics 80, H23–H35. https://doi.org/10.1190/geo2015-0098.1.
Fang, G.Y., Zhou, B., Ji, Y.C., Zhang, Q.Y., Shen, S.X., Li, Y.X., et al., 2014. Lunar penetrating radar onboard the Chang'E-3 mission. Res. Astron. Astrophys. 14 (12), 1607–1622. https://doi.org/10.1088/1674-4527/14/12/009.
Feng, J., Siegler, M.A., White, M.N., 2022. Dielectric properties and stratigraphy of regolith in the lunar South Pole-Aitken basin: observations from the lunar penetrating radar. Astron. Astrophys. 661, A47. https://doi.org/10.1051/0004-6361/202143015.
Feng, J., Siegler, M.A., Su, Y., Ding, C., Giannakis, I., 2023. Layered structures in the upper several hundred meters of the moon along the Chang'E-4 rover's first 1, 000-m traverse. J. Geophys. Res. Planets 128 (8). https://doi.org/10.1029/2022JE007714 e2022JE007714.
Fernandes, V., Fritz, J., Weiss, B., Garrick-Bethell, I., Shuster, D., 2013. The bombardment history of the moon as recorded by ^{40Ar}-^{39Ar} chronology. Meteorit. Planet. Sci. 48 (2), 241–269. https://doi.org/10.1111/maps.12054.
Forte, E., Pipan, M., Casabianca, D., Di Cuia, R., Riva, A., 2012. Imaging and characterization of a carbonate hydrocarbon reservoir analogue using GPR attributes. J. Appl. Geophys. 81, 76–87. https://doi.org/10.1016/j.jappgeo.2011.09.009.
Forte, E., Roncoroni, G., Pipan, M., 2023. Are Lunar Penetrating Radar Data So Unusual? Some Relevant Issues about their Processing and Analysis, 11th European Lunar Symposium, June 27–29, 2023, Padua, Italy.
Fortezzo, C.M., Spudis, P.D., Harrel, S.L., 2020. Release of the digital unified global geologic map of the moon at 1:5,000,000. In: 51st Lunar and Planetary Science Conference, Lunar and Planetary Institute, Houston, TX.
Giannakis, I., Zhou, F., Warren, C., Giannopoulos, A., 2021. Inferring the shallow layered structure at the Chang'E-4 landing site: a novel interpretation approach using Lunar Penetrating Radar. Geophys. Res. Lett. 48 (16) https://doi.org/10.1029/2021GL092866 e2021GL092866.
Giannakis, I., Martin-Torres, J., Su, Y., Feng, J., Zhou, F., Zorzano, M.P., et al., 2024. Evidence of shallow basaltic lava layers in Von Kármán crater from Yutu-2 Lunar Penetrating Radar. Icarus 408, 115837. https://doi.org/10.1016/j.icarus.2023.115837.
Gou, S., Zongyu, Y., Kaichang, D., Zhanchuan, C., Zhaoqin, L., Shengli, N., 2021. Absolute model age of lunar Finsen crater and geologic implications. Icarus 354, 114046. https://doi.org/10.1016/j.icarus.2020.114046.
Guo, D., Fa, W., Zeng, X., Du, J., Liu, J., 2021. Geochemistry of the Von Kármán crater floor and thickness of the non-mare ejecta over the Chang'E-4 landing area. Icarus 359, 114327. https://doi.org/10.1016/j.icarus.2021.114327.
Hochreiter, S., Schmidhuber, J., 1997. Long short-term memory. Neural Comput. 9, 1735–1780. https://doi.org/10.1162/neco.1997.9.8.1735.
Huang, J., Xiao, Z., Flahaut, J., Martinot, M., Head, J., Xiao, X., et al., 2018. Geological characteristics of Von Kármán crater, northwestern south pole-Aitken basin: Chang'E-4 landing site region. J. Geophys. Res. Planets 123 (7), 1684–1700. https://doi.org/10.1029/2018JE005577.
Ivanov, B.A., 2018. Size-frequency distribution of small lunar craters: widening with degradation and crater lifetime. Sol. Syst. Res. 52 (1), 1–25. https://doi.org/10.1134/S0038094618010021.
Jia, Y., Zou, Y., Ping, J., Xue, C., Yan, J., Ning, Y., 2018. The scientific objectives and payloads of Chang'E−4 mission. Planets Space Sci. 162, 207–215. https://doi.org/10.1016/j.pss.2018.02.011.
Jiao, Y., McMechan, G.A., Pettinelli, E., 2000. In situ 2-D and 3-D measurements of radiation patterns of half-wave dipole GPR antennas. J. Appl. Geophys. 43 (1), 69–89. https://doi.org/10.1016/S0926-9851(99)00048-8.
Jol, H.M., 2009. Ground Penetrating Radar Theory and Applications. Elsevier. B978-0-444-53348-7. 00016-8.
Lai, J., Xu, Y., Bugiolacchi, R., Meng, X., Xiao, L., Xie, M., et al., 2020. First look by the Yutu-2 rover at the deep subsurface structure at the lunar farside. Nat. Commun. 11 (1), 3426. https://doi.org/10.1038/s41467-020-17262-w.
Lai, J., Xu, Y., Bugiolacchi, R., Wong, H.K., Xu, L., Zhang, X., et al., 2021. A complex paleo-surface revealed by the Yutu-2 rover at the lunar farside. Geophys. Res. Lett. 48 (20) https://doi.org/10.1029/2021GL095133 e2021GL095133.
Li, C., Xing, S., Lauro, S.E., Su, Y., Dai, S., Feng, J., et al., 2018. Pitfalls in GPR data interpretation: false reflectors detected in lunar radar cross sections by Chang'e-3. IEEE Trans. Geosci. Remote Sens. 56 (3), 1325–1335. https://doi.org/10.1109/TGRS.2017.2761881.
Li, C., Su, Y., Pettinelli, E., Shuguo, X., Ding, C., Liu, J., et al., 2020. The Moon's farside shallow subsurface structure unveiled by Chang'E-4 Lunar Penetrating Radar. Sci. Adv. 6 (9) https://doi.org/10.1126/sciadv.aay6898 eaay 6898.
Lin, H., Lin, Y., Yang, W., He, Z., Hu, S., Wei, Y., et al., 2020. New insight into lunar regolith-forming processes by the Lunar Rover Yutu-2. Geophys. Res. Lett. 47 https://doi.org/10.1029/2020GL087949 e2020GL087949.
Ling, Z., Qiao, L., Liu, C., Cao, H., Bi, X., Lu, X., et al., 2019. Composition, mineralogy and chronology of mare basalts and non-mare materials in Von Kármán crater: landing site of the Chang'E−4 mission. Planet. Space Sci. 179, 104741 https://doi.org/10.1016/j.pss.2019.104741.
Liu, H., Wang, S., Jing, G., Yu, Z., Yang, J., Zhang, Y., et al., 2023. Combined CNN and RNN neural networks for GPR detection of railway subgrade diseases. Sensors 23, 5383. https://doi.org/10.3390/s23125383.
Lu, Y., Wu, Y., Michael, G.G., Ma, J., Cai, W., Qin, N., 2021. Chronological sequence of Chang'E-4 landing zone within Von Kármán crater. Icarus 354, 114086. https://doi.org/10.1016/j.icarus.2020.114086.
Mannor, S., Peleg, D., Rubinstein, R., 2005. The cross entropy method for classification. In: Proceedings of the 22nd International Conference on Machine Learning - ICML '05. ACM Press, pp. 561–568. https://doi.org/10.1145/1102351.1102422.
Marco Figuera, R., Riedel, C., Rossi, A.P., Unnithan, V., 2022. Depth to diameter analysis on small simple craters at the Lunar South Pole—possible implications for ice harboring. Remote Sens. 14, 450. https://doi.org/10.3390/rs14030450.
Melosh, H.J., 1989. Impact Cratering: A Geologic Process. Oxford University Press.
Mendes-Moreira, J., Jorge, A.M., Soares, C., de Sousa, J.F., 2009. Ensemble learning: a study on different variants of the dynamic selection approach. In: Perner, P. (Ed.), Machine Learning and Data Mining in Pattern Recognition. Springer Berlin Heidelberg, pp. 191–205.
Neto, P.S., Medeiros, W.E., 2006. A practical approach to correct attenuation effects in GPR data. J. Appl. Geophys. 59 (2), 140–151. https://doi.org/10.1016/j.jappgeo.2005.09.002.
Oliveros, R.B., Radovich, B.J., 1997. Image-processing display techniques applied to seismic instantaneous attributes over the Gorgon Gas Field, North West Shelf, Australia. In: Society of Exploration Geophysics, SEG Technical Program Expanded Abstracts (2064–2067). https://doi.org/10.1190/1.1885862.
Pettinelli, E., Lauro, S.E., Mattei, E., Cosciotti, B., Soldovieri, F., 2021. Stratigraphy versus artefacts in the Chang'e-4 low-frequency radar. Nat. Astron. 5 (9), 890–893. https://doi.org/10.1038/s41550-021-01432-x.
Roncoroni, G., Forte, E., Bortolussi, L., Pipan, M., 2022a. Efficient extraction of seismic reflection with deep learning. Comput. Geosci. 166, 105190 https://doi.org/10.1016/j.cageo.2022.105190.
Roncoroni, G., Forte, E., Bortolussi, L., Gasperini, L., Pipan, M., 2022b. Polarity assessment of reflection seismic data: a deep learning approach. Bull. Geophys. Oceanogr. 63, 693–700. https://doi.org/10.4430/bgo00409.
Roncoroni, G., Forte, E., Santin, I., et al., 2024. High frequency Lunar Penetrating Radar quality control, editing and processing of Chang'E-4 lunar mission. Sci. Data 11, 118. https://doi.org/10.1038/s41597-024-02963-4.
Sénéchal, P., Perroud, H., Sénéchal, G., 2000. Interpretation of reflection attributes in a 3-D GPR survey at Vallée d'Ossau, western Pyrenees, France. Geophysics 65 (5), 1435–1445. https://doi.org/10.1190/1.1444832.
Wang, R., Su, Y., Ding, C., Dai, S., Liu, C., Zhang, Z., et al., 2021. A novel approach for permittivity estimation of lunar regolith using the Lunar Penetrating Radar onboard Chang'E-4 Rover. Remote Sens. 13 (18), 3679. https://doi.org/10.3390/rs13183679.
Warner, N.H., Golombek, M., Sweeney, J., Fergason, R., Kirk, R., Schwartz, C., 2017. Near surface stratigraphy and regolith production in Southwestern Elysium Planitia, Mars: implications for Hesperian-Amazonian Terrains and the InSight Lander Mission. Space Sci. Rev. 211 (1–4), 147–190. https://doi.org/10.1007/s11214-017-0352-x.
White, L.F., Cernok, A., Darling, J., Whitehouse, M., Joy, K., Cayron, C., et al., 2020. Evidence of extensive lunar crust formation in impact melt sheets 4,330 Myr ago. Nat. Astron. 4 (10), 974–978. https://doi.org/10.1038/s41550-020-1092-5.
Wu, W., Li, C., Zuo, W., Zhang, H., Liu, J., Wen, W., et al., 2019. Lunar farside to be explored by Chang'E-4. Nat. Geosci. 12 (4), 222–223. https://doi.org/10.1038/s41561-019-0341-7.
Xiao, Z., Ding, C., Xie, M., Cai, Y., Cui, J., Zhang, K., Wang, J., 2021. Ejecta from the Orientale Basin at the Chang'E-4 landing site. Geophys. Res. Lett. 48 (3) https://doi.org/10.1029/2020GL090935 e2020GL090935.
Xu, C., Zhang, G., Zhang, J., Jia, Z., 2020. Time–frequency attribute analysis of channel 1 data of lunar penetrating radar. Appl. Sci. 10 (2), 535. https://doi.org/10.3390/app10020535.
Xu, L., Zhang, X., Qiao, L., Lai, J., 2021. Evaluating the thickness and stratigraphy of ejecta materials at the Chang'e-4 landing site. Astron. J. 162 (1), 29. https://doi.org/10.3847/1538-3881/abf8b0.
Yang, L., Sun, S.Z., 2019. Seismic horizon tracking using a deep convolutional neural network. J. Pet. Sci. Eng. 187, 1–15. https://doi.org/10.1016/j.petrol.2019.106709.
Yilmaz, Ö., 2001. Seismic Data Analysis: Processing, Inversion, and Interpretation of Seismic Data, , 2ed.Vol.10. Society of Exploration Geophysicists. https://doi.org/10.1190/1.9781560801580.
Zhang, L., Li, J., Zeng, Z., Xu, Y., Liu, C., Chen, S., 2020. Stratigraphy of the Von Kármán crater based on Chang'E-4 lunar penetrating radar data. Geophys. Res. Lett. 47 (15) https://doi.org/10.1029/2020GL088680.
Zhang, L., Xu, Y., Bugiolacchi, R., Hu, B., Liu, C., Lai, J., et al., 2021a. Rock abundance and evolution of the shallow stratum on Chang'E-4 landing site unveiled by Lunar Penetrating Radar data. Earth Planet. Sci. Lett. 564, 116912 https://doi.org/10.1016/j.epsl.2021.116912.
Zhang, J., Zhou, B., Lin, Y., 2021b. Reply to: stratigraphy versus artefacts in the Chang'e-4 low-frequency radar. Nat. Astron. 5, 894–897. https://doi.org/10.1038/s41550-021-01432-x.
Zhao, W., Forte, E., Fontana, F., Pipan, M., Tian, G., 2018. GPR imaging and characterization of Ancient Roman ruins in the Aquileia Archaeological Park, NE Italy. Measurement 113, 161–171. https://doi.org/10.1016/j.measurement.2017.09.004.

Zhou, H., Feng, X., Dong, Z., Liu, C., Liang, W., 2021. Application of denoising CNN for noise suppression and weak signal extraction of Lunar Penetrating Radar data. Remote Sens. 13 (4), 779. https://doi.org/10.3390/rs13040779.

Zhou, H., Feng, X., Ding, C., Dong, Z., Liu, C., Liang, W., 2022a. Heterogeneous weathering process of lunar regolith revealed by polarimetric attributes analysis of Chang'E-4 Lunar Penetrating Radar data acquired during the Yutu-2 turnings. Geophys. Res. Lett. 49 (13) https://doi.org/10.1029/2022GL099207 e2022GL099207.

Zhou, H., Feng, X., Ding, C., Dong, Z., Liu, C., Zhang, Y., Meng, Z., 2022b. Yutu-2 radar sounding evidence of a buried crater at Chang'E-4 landing site. IEEE Trans. Geosci. Remote Sens. 60, 1–19. https://doi.org/10.1109/TGRS.2021.3090528.

Zhu, D., Shi, Z., Wang, X., Chen, A., 2021. High-resolution GPR horizon extraction method based on local reflection and global correlation. IOP Conf. Ser. Earth Environ. Sci. 660, 012025 https://doi.org/10.1088/1755-1315/660/1/012025.